Electronic Supplementary Material (ESI) for Journal of Materials Chemistry A.

Supporting Information

Dynamic but Mechanically Robust and Ultrafast Healable Ionogel for Nerve Fiber-inspired Signal Transmitter

Ping Liu,[a,b,#] Danfeng Pei,*[b,c,#] Yongpeng Wu,[b] Mingjie Li,[b,c] Xihui Zhao,*[a] Chaoxu Li*[b,c]

[a]College of Chemistry and Chemical Engineering, Qingdao University, 308 Ningxia Road, Qingdao, Shandong 266071, P. R. China

[b]Group of Biomimetic Smart Materials, Qingdao Institute of Bioenergy and Bioprocess Technology, CAS & Shandong Energy Institute, Songling Road 189, Qingdao 266101, P. R. China

[c]Center of Material and Optoelectronics Engineering, University of Chinese Academy of Sciences, 19A Yuquan Road, Beijing 100049, P. R. China

[#]The authors made equal contributions to this work

Corresponding Authors

E-mail: licx@qibebt.ac.cn, peidf@qibebt.ac.cn, zhaoxihui@qdu.edu.cn

Synthesis of diselenpropionic acid dimethylester

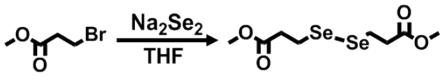

Disodium diselenide was prepared through reaction between Se powder and sodium borohydride in water. 3,3´-diseleniumpropionic acid dimethylester was synthesized through the reaction between disodium diselenide and methyl 3-bromopropanoate in THF at 50°C. The product was purified by column chromatography with a 10:1 mixture of petroleum ether and ethyl acetate as eluent and yellow oil was obtained with a yield of 60%.[1]H NMR was shown in Fig. S1A

Synthesis of 3,3'-diselanediyldi(propanehydrazide)

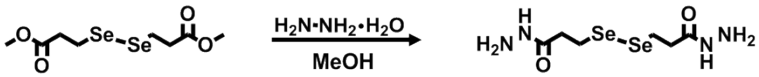

The 3,3´-diselendipropionic acid dihydrazide was synthesized according to previous literature.[1] 3,3´-diselenpropionic acid dimethylester (2 g, 6 mmol) was dissolved in dry MeOH (5 mL). Hydrazine hydrate (1.8 g, 36 mmol, 6 equiv) was added and the mixed reactant was stirred at 30 °C for 12 h. The resulting suspension was filtered, and the white solid was washed using water (2 mL) and MeOH (10 mL), respectively. The product was obtained (1.3 g, yield: 65%). [1]H NMR (600 MHz, DMSO-d_6, δppm, Fig.S1B), 9.07 (s, 2H, N-NH-C(O)), 4.21 (s, 4H, NH_2-N-C(O)), 2.89 (t, 4H, C(O)-C-CH_2-), 2.42 (t, 4H, N-C(O)-CH_2-C).

Tensile tests

True stress (σ_t) and true strain (ε_t) are calculated based on the engineering stress-strain curves, measured at the stretching speed of 50 mm min^{-1}, by the following equation:

$\sigma_t = \sigma * L/L_0 = \sigma * (\varepsilon + 1)$

$\varepsilon_t = \int dL/L = lnL/L_0 = ln\ (\varepsilon + 1)$

where σ is the engineering stress, L is the instant length of the deformed specimen, L_0 is the original length of the specimen, ε is the engineering strain.

Tensile toughness of the samples can be defined by integrating the area under the engineering stress (σ)-strain (ε) curves, measured at the stretching speed of 50 mm min^{-1}.

Mechanical robustness of PUSe

Mechanical properties of the supramolecular PUSe were measured via tensile tests, and the typical engineering stress–strain curves were shown in Fig. S9A. With the increasing of acylsemicarbazide and urethane moieties, the tensile strength of PUSe increased but the toughness gradually decreased. The increased of hard segments was accompanied by an increasing amount of H-bonding density which resulted in the stiffer PUSe. The $PUSe_{0.3}$ elastomer exhibited a tensile strength (i.e., ultimate engineering stress) of 36.3 MPa and a toughness of 142.5 MJ m^{-3} (Fig. S9B).

Cyclic tensile tests were carried out to study the elastic restorability of the PUSe. Fig. S9C showed the cyclic loading–unloading tensile curves of the elastomer at the strain of 200%, measured at different waiting times between two consecutive loading-unloading cycles. The first loading-unloading curve demonstrated a pronounced hysteresis loop (4.64 MJ m^{-3}), indicating the substantial energy dissipation due to the force-induced rupture of the H-bonds. With the increase of waiting time, the loading–unloading curves and hysteresis loop gradually recovered and nearly reached the original state after a waiting time of 30 min.

Ultrafast-healability of PUSe

Benefitted from the rapid diselenide metathesis and the dynamic H-bond rupture and reformation in the H-bond arrays, the superstrong, ultratough, and dynamic PUSe was ultrafast healable. As shown in Fig. S16, depicted the healing efficiency of the $PUSe_{0.3}$, in terms of the tensile strength, as a function of the healing time and light intensity, respectively. The healing efficiency increased with the light intensity and time. The healing efficiency of fractured $PUSe_{0.3}$ can reach 60% after healing at 3.0 W cm^{-2} for 30 s and a 90% healing achieved for 5.0 W cm^{-2} irradiation in 30 s for both the tensile strength and elongation-at-break. The ultrafast healing mechanism may come from the synergy of the dense hydrogen-bond arrays and the rapid diselenide exchange in PUSe. When the damaged PUSe was irradiated under visible light, the dynamic exchange of diselenide bonds occurred. Meanwhile, the elevated temperature enabled the hydrogen-bond arrays dynamically disintegrate. Thus, polymer chain mobility was significantly enhanced. When the two fractured surfaces were in contact, the polymer chains on the fractured surfaces diffused toward each other, the diselenide metathesis continuously proceeded and the hydrogen-bond-cross-linked network rebuilt. The diselenide bond and hydrogen-bond arrays reformed in the PUSe interfaces after the irradiation. As a result, the integrity and mechanical properties of the fractured PUSe were finely restored.

Tunable structural color patterns based on dynamic diselenide metathesis of PUSe

In the supramolecular PUSe, the stress could be regulated by diselenide metathesis under visible light irradiation, further insight into the birefringence of this PUSe was

sought. As shown in Fig. S25, with the increase of strain, the transmitted wavelength showed an intense redshift from 490 to 710 nm. On the other hand, during the stress relaxation (480 nm irradiation, 0.04 W cm^{-2}), the transmitted wavelength showed a strong blueshift with the increase of releasing time.

The mechanism of chromatic polarization

As shown in Scheme S1, the polarization of P1 is orthogonal to P2. The linearly polarized light from P1 is refracted as it passes through the stretched material, which generates two beams with a phase difference (Fig. S20A). The two beams have the same propagating direction but with different speeds, causing a phase delay. They interfere in the polarized direction of P2, which forms a structural color (Fig. S20B). The wavelength of destructive interference, whose phase difference is π, is related to the stress and the thickness of the material (Equation S1). The optical axis is parallel to the stretching direction. A maximum light intensity is achieved when the angle of optical axis and polarized direction reaches 45° (Equation S2).

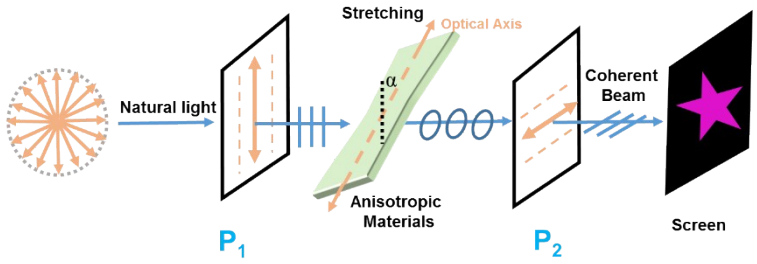

Scheme S1. Scheme for the mechanism of tunable structural color based on controllable stress relaxation and birefringence under polarized light.

Supporting figures

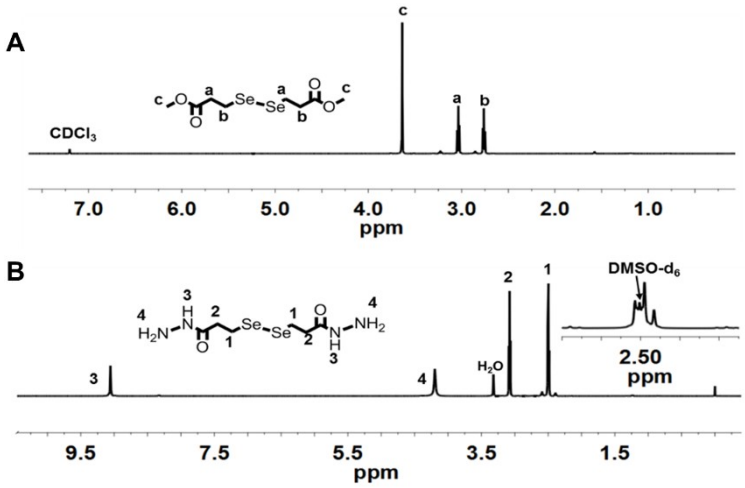

Figure S1 ^{1}H NMR spectra of diselenpropionic acid dimethylester in $CDCl_3$ (A) and 3,3'-diselanediyldi(propanehydrazide) in DMSO-d6 (B) at 25ºC.

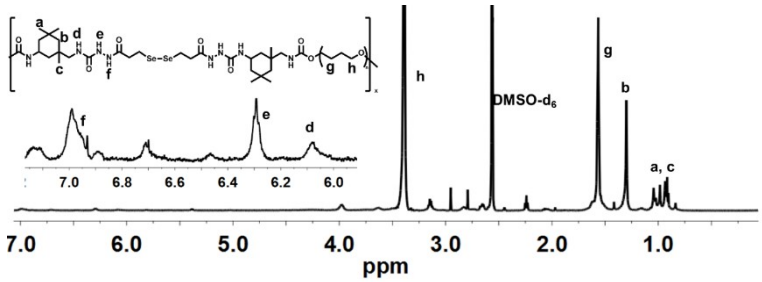

Figure S2 ^{1}H NMR spectra of $PUSe_{0.3}IL_{0.2}$ in DMSO-d_6 at 25ºC.

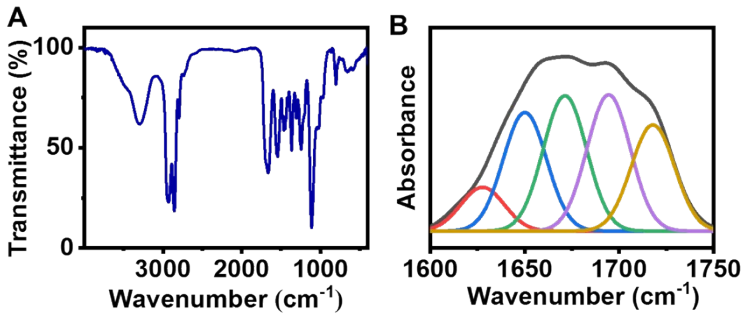

Figure S3 (A, B) FTIR spectra of $PUSe_{0.3}IL_{0.2}$ at 25ºC.

Table S1 Summary of the assignment of the deconvoluted subpeaks in the FTIR C=O absorption bands for the $PUSe_{0.3}IL_{0.2}$.

Assignments	**Wavenumber (cm^{-1})**	**Area (%)**	**Total degree of H-bonded (%)**
free ν (C=O) urethane amide	1715	19.6	
H-bonded ν (C=O) urethane amide	1704	25.3	
free ν (C=O) urea amide	1696	25.1	55.4
H-bonded ν (C=O) urea amide	1665	22.0	
H-bonded ν (C=O) amide	1639	8.1	

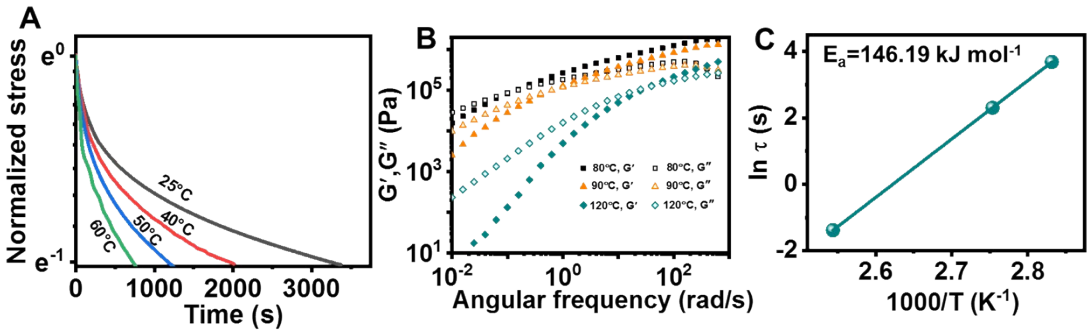

Figure S4 (A) Normalized stress relaxation curves over time at different temperature of $PUSe_{0.3}IL_{0.2}$. (B) Storage shear modulus G′ and loss shear modulus G″ as functions of angular frequency at different sweeping temperatures in $PUSe_{0.3}IL_{0.2}$. (C) Corresponding Arrhenius plots derived from the relaxation times.

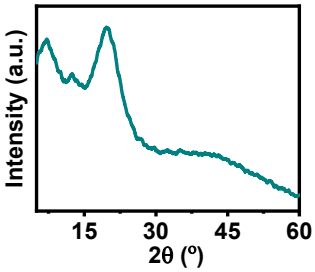

Figure S5 XRD spectrum of $PUSe_{0.3}IL_{0.2}$.

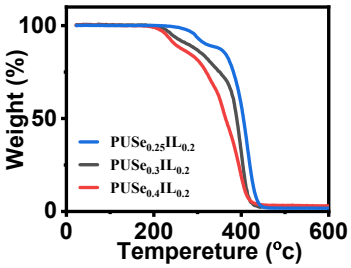

Figure S6 TGA spectrum of PUSeIL.

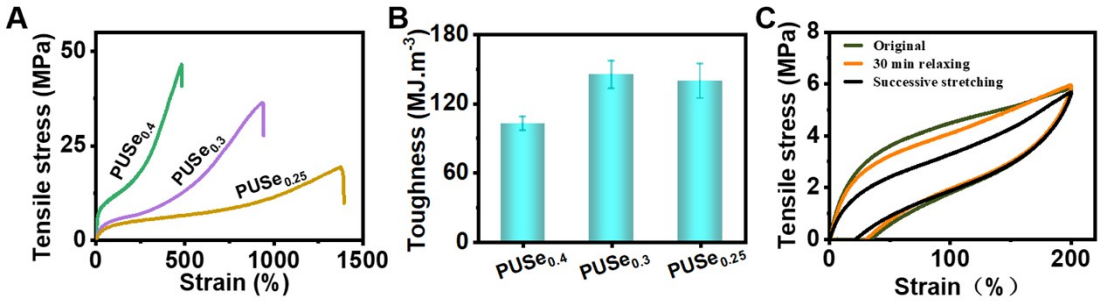

Figure S7 **Mechanical characterization of PUSe.** (A) Tensile stress-strain curves with indicated segmental ratios. (B) Toughness of PUSeIL with indicated segmental ratios. (C) Cyclic tensile curves of $PUSe_{0.3}$with indicated relaxing time.

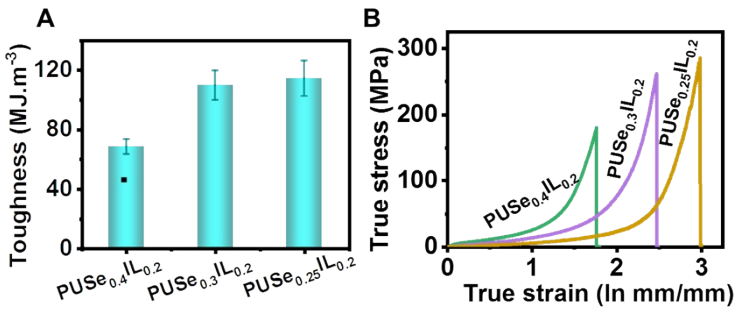

Figure S8 (A) Toughness of PUSeIL with indicated segmental ratios. (B) True stress–strain curves of the PUSeIL.

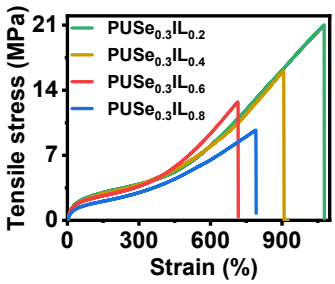

Figure S9 Tensile stress-strain curves with indicated segmental ratios.

Table S2 Comparisons of mechanical properties with reported conductives.

	Materials	Toughness ($MJ.cm^{-3}$)	Breaking strength （MPa）	Reference
Solid electrolyte	CHPE	1.92	3.2	2
	xPTHF SPE	0.3	1.2	3
	PEDOT: PSS-NR	27	6.5	4
	ICE	12	1.5	5
Conductive hydrogels	PAni-PAAm GOCS	4.75	1.9	6
	LmSn	3	0.3	7
	P(urea-IL_1-$SPMA_1$)-3d	4.9	1.4	8
Ionogel	IG	28	2.1	9
	ICEC	17	7	10
	PU-Zn-IL	117.7	15.2	11
	$PVA/PVP_m/IL_n$	32	7.7	12
	$PU\text{-}IL_2$	2.5	2.5	13
		67.2	31	**This work**
		109.4	22	
		114.9	15	

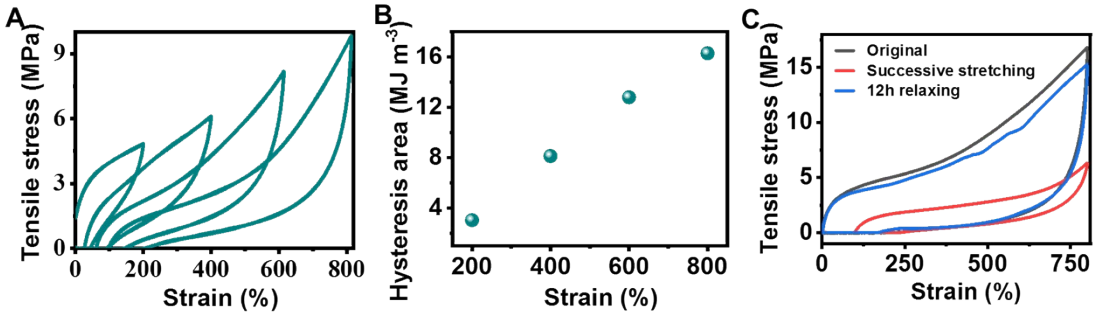

Figure S10 (A) Cyclic tensile curves with different strain. (B) Corresponding hysteresis area at each loading–unloading cycle. (C) Cyclic tensile curves of $PUSe_{0.3}IL_{0.2}$.

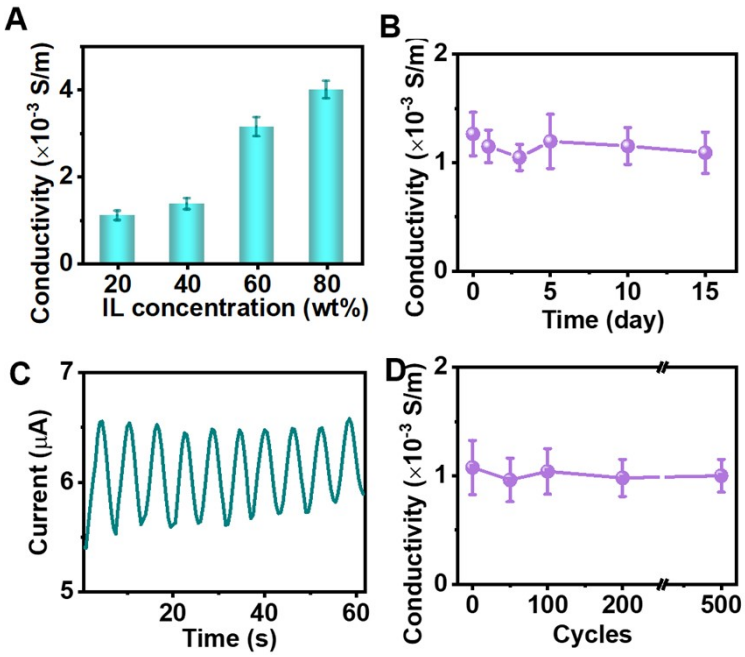

Figure S11 (A) Conductivity of $PUSe_{0.3}IL_y$ with different IL content. (B) Conductivity of $PUSe_{0.3}IL_{0.2}$ with increasing storage time. (C) The varying current signal during stretching-releasing cycles with the maximal strain of 100%. (D) The ionic conductivity of $PUSe_{0.3}IL_{0.2}$ cyclic tensile with the maximal strain of 100%.

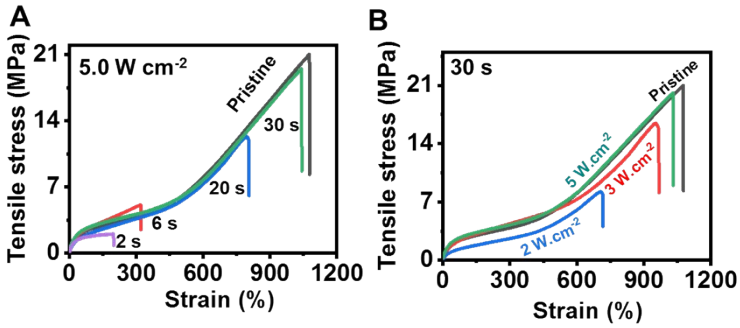

Figure S12 (A) Stress-strain curves after healing for indicated time periods under 5.0 W cm^{-2} irradiation of $PUSe_{0.3}IL_{0.2}$. (B) Stress-strain curves after healing for 30 s under different light power of $PUSe_{0.3}IL_{0.2}$.

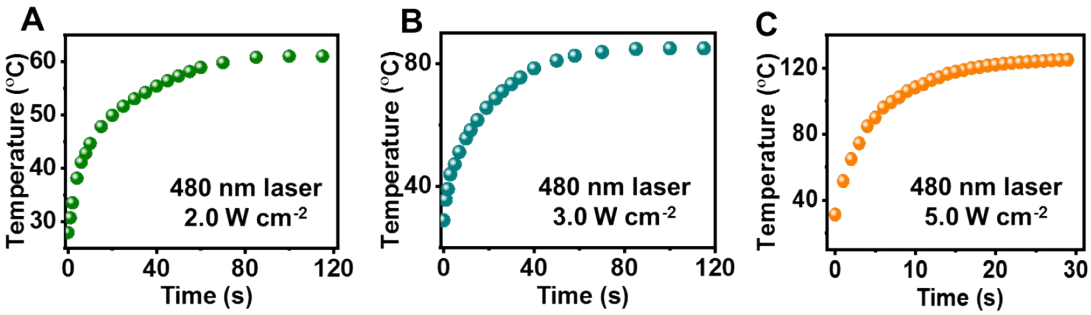

Figure S13 Temperature-time diagram under indicated visible light irradiation (A) 2.0 W cm^{-2}. (B) 3.0 W cm^{-2}. (C) 5.0 W cm^{-2}.

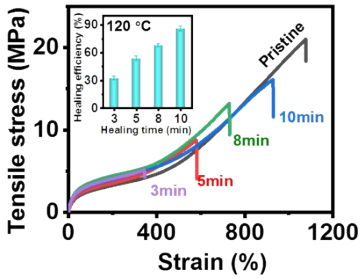

Figure S14 (A) Stress-strain curves after healing for indicated time periods at 120ºC of $PUSe_{0.3}IL_{0.2}$.

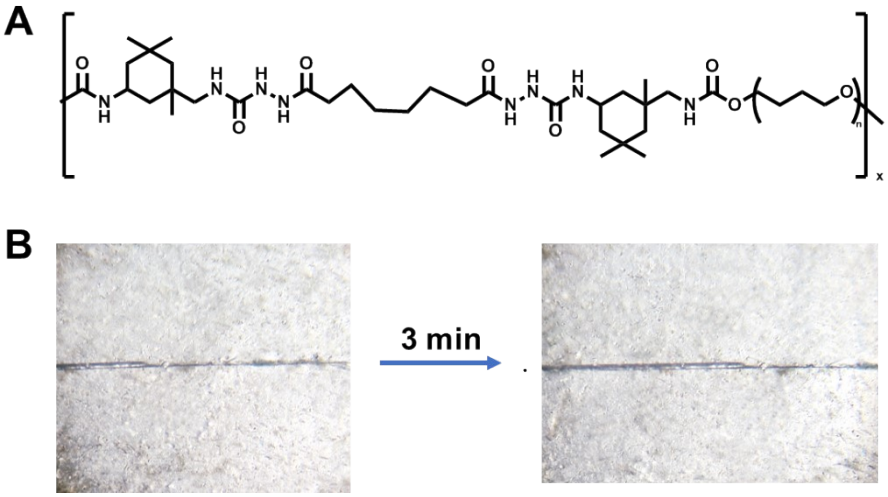

Figure S15 (A) The structure of the controlled ionogel in which dihydrazide diselenide was replaced by adipic dihydrazide. (B) Visual observation of cross-sectionally cutting then healed for 3 min under visible light (12.0 W cm^{-2}).

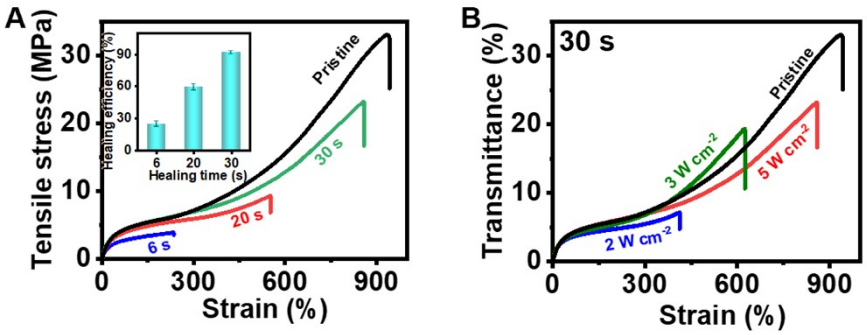

Figure S16 (A) Stress-strain curves after healing for indicated time periods under 5.0 W cm^{-2} irradiation and the healing efficiency (insert) of $PUSe_{0.3}$. (B) Stress-strain curves after healing for 30 s under different light power of $PUSe_{0.3}$.

Table S3 Comparisons of self-healing properties.

	Materials	Breaking strength (MPa)	Healing time	Reference
Hydrogel	2.1-7/3 hydrogel	0.5	5 min	14
	LmSn	0.27	24 h	7
	P(urea-IL_1-$SPMA_1$)-3d	1.3	28 h	8
	NAGA	1.1	30 min	15
	UPyHCBA	0.45	30 s	16
	freeze–thawed hydrogels	3.2	50 min	17
Elastomer	PPGTD-IDA	5	48h	18
	PDM-2.5	30	24 h	19
	poly(urea–urethane)	0.8	24 h	20
	TPU	6.8	2 h	21
	Cu-DOU-CPU	15	130 h	22
	TPU	48	48 h	23
Ionogel	SDA ion gel	0.3	180 min	24
	Cel-IL	0.9	3 h	25
	I-Skin	0.9	10 s	26
	EMIOTf	0.3	30 min	27
Ionogel	PU-Zn-IL	15.2	2 h	11
	PU-IL_2	2.5	3 h	13
		22	30 s	**This work**

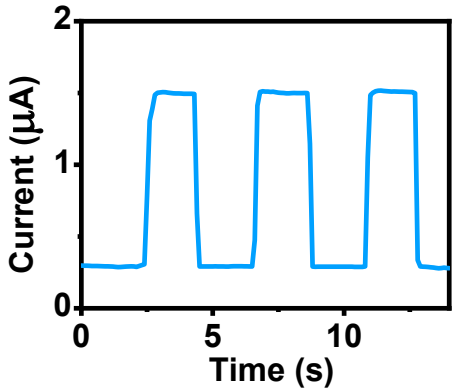

Figure S17 Real-time current during cyclic cutting and healing processes under voltage bias of 2 V of $PUSe_{0.3}IL_{0.2}$.

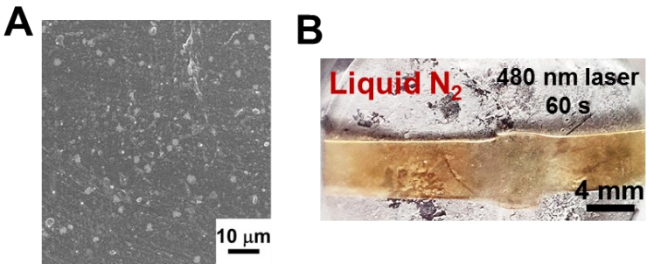

Figure S18 (A) SEM of the interface between two welded $PUSe_{0.3}IL_{0.2}$ films. (B) Visual observation of two $PUSe_{0.3}IL_{0.2}$ films welded in liquid N_2 surroundings for 60 s under visible light (12.0 W cm^{-2}).

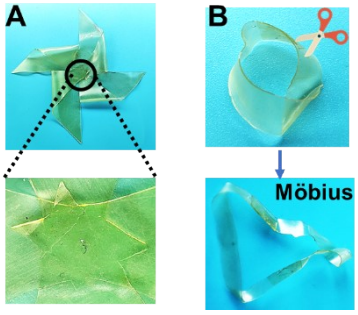

Figure S19 Visual observation of two $PUSe_{0.3}IL_{0.2}$ films welded (A) pinwheel. (B)Möbius ring.

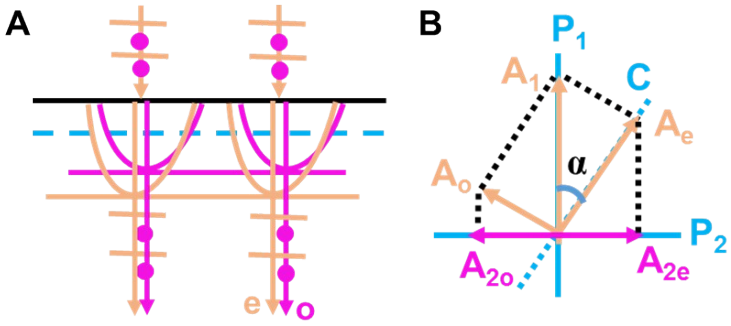

Figure S20 Mechanism of chromatic polarization. (A) The “o” represents the ordinary light. The “e” represents the extraordinary light. Light blue dotted lines represent optic axis. Purple dots represent that the polarized direction of ordinary light is perpendicular to the optic axis. Orange dashes represent that the polarized direction of extraordinary

light is parallel to the optic axis. (B) A_{2e} is the component of A_e along the polarized direction of P_2 while A_e is the amplitude of extraordinary light. Similarly, A_{2o} is the component of A_o (the amplitude of ordinary light) along the polarized direction of P_2.

The calculation of phase difference between A_{2O} and A_{2e} is shown in Equation S1, where $|\Delta\varphi|$ represents the phase difference between A_{2o} and A_{2e}. $|\Delta\varphi_c|$ represents the phase difference between A_o and A_e. The n_o is the refractive index of ordinary light. The n_e is the refractive index of extraordinary light. The d is thickness of material. The λ is the wavelength of transmitted light.

$$|\Delta\varphi| = |\Delta\varphi c| + \pi = |n_o - n_e| \times d \times 2\pi/\lambda + \pi \quad \text{(S1)}$$

when $|\Delta\varphi|$ equals $2k\square$ (k = 0, 1, 2, 3⋯), the sum of A_{2o} and A_{2e} is calculated by Equation S2.

$$|A_{2o}| + |A_{2e}| = 2 \times A_1 \sin\alpha \cos\alpha = A_1 \sin 2\alpha \quad \text{(S2)}$$

When α equals 45°, the sum of A_{2o} and A_{2e} reaches maximum and the structural color is brightest.

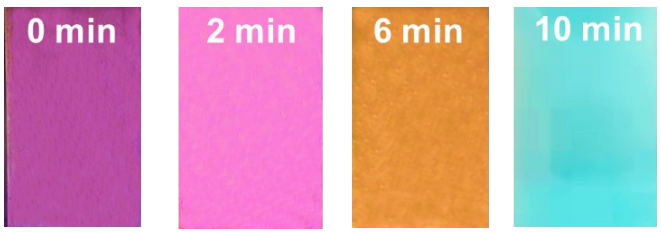

Figure S21 The colored $PUSe_{0.3}IL_{0.2}$ film under polarized light after irradiated for different time (0.04 W cm^{-2}).

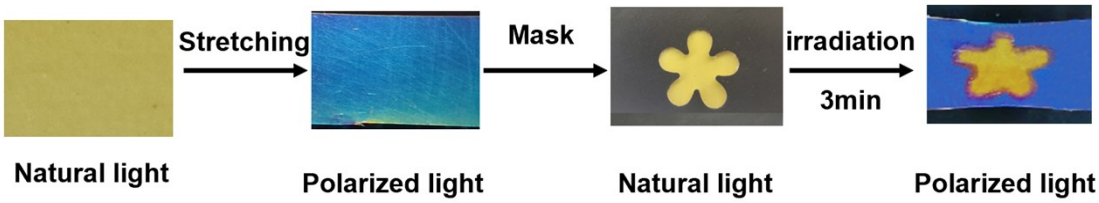

Figure S22 The procedure for realizing the structural color pattern in PUSeIL.

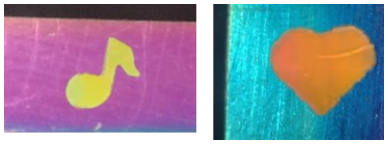

Figure S23 Various patterns with different structural colors realized by photomask.

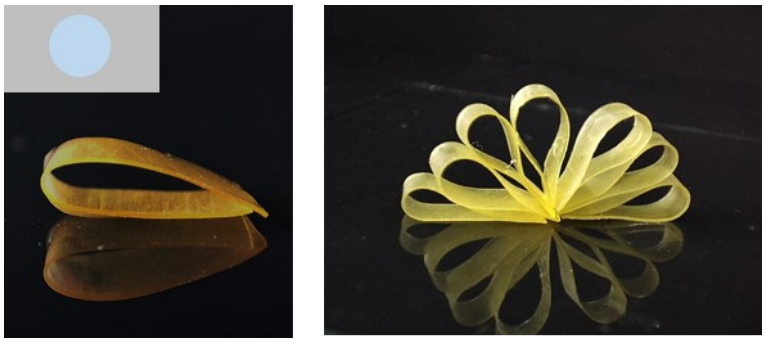

Figure S24 3D shape-morphing of PUSeIL with a circle photomask.

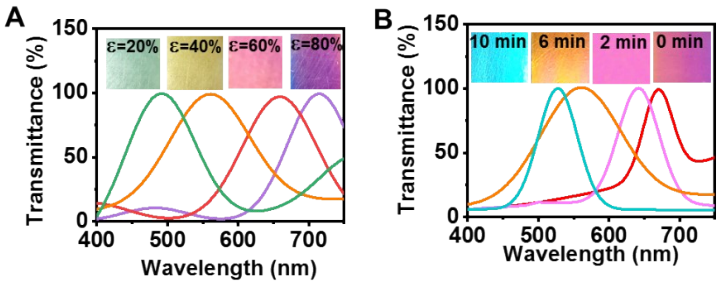

Figure S25 **Tunable structural color of PUSe**. (A) Transmission peak with the indicated strain in $PUSe_{0.3}$. The colored $PUSe_{0.3}$ film under polarized light correspond to the spectral curves below. (B) Blue-shift of the transmission peak with the increase of stress releasing time in $PUSe_{0.3}$.

References

1. N. Xu, B. Wang, Z. An, Y. Liu, L. Liu, Z. Hu and Y. Huang, *Chem. Mater.*, 2022, **34**, 4732-4740.

2. C. Zuo, M. Yang, Z. Wang, K. Jiang, S. Li, W. Luo, D. He, C. Liu, X. Xie and Z. Xue, *J. Mater. Chem. A*, 2019, **7**, 18871-18879.

3. D. G. Mackanic, W. Michaels, M. Lee, D. Feng, J. Lopez, J. Qin, Y. Cui and Z. Bao, *Adv. Energy Mater.*, 2018, **8**, 1800703.

4. Y. Yang, G. Zhao, X. Cheng, H. Deng and Q. Fu, *ACS Appl. Mater. Interfaces*, 2021, **13**, 14599-14611.

5. B. Yiming, Y. Han, Z. Han, X. Zhang, Y. Li, W. Lian, M. Zhang, J. Yin, T. Sun, Z. Wu, T. Li, J. Fu, Z. Jia and S. Qu, *Adv. Mater.*, 2021, **33**, 2006111.

6. X. Jin, H. Jiang, G. Li, B. Fu, X. Bao, Z. Wang and Q. Hu, *Chem. Eng. J.*, 2020, **394**, 124901.

7. L. Wang, G. Gao, Y. Zhou, T. Xu, J. Chen, R. Wang, R. Zhang and J. Fu, *ACS Appl. Mater. Interfaces*, 2019, **11**, 3506-3515.

8. T. Long, Y. Li, X. Fang and J. Sun, *Adv. Funct. Mater.*, 2018, **28**, 1804416.

9. P. Wang, G. Li, W. Yu, C. Meng and S. Guo, *Adv. Mater. Interfaces,* 2022, **9**, 2102426.

10. B. Zhang, Q. Feng, H. Song, X. Zhang, C. Zhang and T. Liu, *ACS Appl. Mater. Interfaces*, 2022, **14**, 8404-8416.

11. X. Wang, Y.-l. Wang, X. Yang, Z. Lu, Y. Men and J. Sun, *Macromolecules*, 2021, **54**, 10767-10775.

12. D. Weng, F. Xu, X. Li, S. Li, Y. Li and J. Sun, *ACS Appl. Mater. Interfaces*, 2020, **12**,

57477-57485.

13. T. Li, Y. Wang, S. Li, X. Liu and J. Sun, *Adv. Mater.*, 2020, **32**, 2002706.

14. Y. Zhang, Q. Hu, S. Yang, T. Wang, W. Sun and Z. Tong, *Macromolecules*, 2021, **54**, 5218-5228.

15. X. Dai, Y. Zhang, L. Gao, T. Bai, W. Wang, Y. Cui and W. Liu, *Adv. Mater.*, 2015, **27**, 3566-3571.

16. I. Jeon, J. Cui, W. R. Illeperuma, J. Aizenberg and J. J. Vlassak, *Adv. Mater.*, 2016, **28**, 4678-4683.

17. Z. Jiang, B. Diggle, I. C. G. Shackleford and L. A. Connal, *Adv. Mater.*, 2019, **31**, 1904956.

18. D. Wang, J. Xu, J. Chen, P. Hu, Y. Wang, W. Jiang and J. Fu, *Adv. Funct. Mater.*, 2019, **30**, 1907109.

19. Y. Li, W. Li, A. Sun, M. Jing, X. Liu, L. Wei, K. Wu and Q. Fu, *Mater. Horiz.*, 2021, **8**, 267-275.

20. A. Rekondo, R. Martin, A. Ruiz de Luzuriaga, G. Cabañero, H. J. Grande and I. Odriozola, *Mater. Horiz.*, 2014, **1**, 237-240.

21. S. M. Kim, H. Jeon, S. H. Shin, S. A. Park, J. Jegal, S. Y. Hwang, D. X. Oh and J. Park, *Adv. Mater.*, 2018, **30**, 1705145.

22. L. Zhang, Z. Liu, X. Wu, Q. Guan, S. Chen, L. Sun, Y. Guo, S. Wang, J. Song, E. M. Jeffries, C. He, F. L. Qing, X. Bao and Z. You, *Adv. Mater.*, 2019, **31**, 1901402.

23. Y. Eom, S. M. Kim, M. Lee, H. Jeon, J. Park, E. S. Lee, S. Y. Hwang, J. Park and D. X. Oh, *Nat. Commun.*, 2021, **12**, 621.

24. R. Tamate, K. Hashimoto, T. Horii, M. Hirasawa, X. Li, M. Shibayama and M. Watanabe, *Adv. Mater.*, 2018, **30**, 1802792.

25. D. Zhao, Y. Zhu, W. Cheng, G. Xu, Q. Wang, S. Liu, J. Li, C. Chen, H. Yu and L. Hu, *Matter*, 2020, **2**, 390-403.

26. S. Hao, T. Li, X. Yang and H. Song, *ACS Appl. Mater. Interfaces*, 2022, **14**, 2029-2037.

27. Y. Cao, T. G. Morrissey, E. Acome, S. I. Allec, B. M. Wong, C. Keplinger and C. Wang, *Adv. Mater.*, 2017, **29**, 1605099.